Journal of Materials Chemistry A

ROYAL SOCIETY OF CHEMISTRY

COMMUNICATION

View Article Online
View Journal | View Issue

Cite this: J. Mater. Chem. A, 2026, 14, 20058

Received 27th March 2026
Accepted 8th May 2026

DOI: 10.1039/d6ta02632j

rsc.li/materials-a

Magnetic-field-assisted cascade electrocatalysis: simultaneous H_2O_2 generation and $^{\cdot}OH$ radical production for coupled hydrogen evolution and water disinfection

Yeonsu Han,†[a] Jungsue Choi,†[a] Soyun Oh,†[a] Hyun Ko[b] and Hyoyoung Lee *abc

Current research on green hydrogen mainly focuses on water electrolysis. However, the low commercial utility of oxygen hinders the reduction of hydrogen production costs. Herein, we report a bifunctional Mn-SnO_2@Fe_3O_4 catalyst for simultaneous hydrogen production and water disinfection. Under an external magnetic field, the system triggers a cascade reaction, converting *in situ* generated H_2O_2 into $^{\cdot}OH$ radicals *via* a Fenton-like reaction. This synergy achieved 99.9% antibacterial efficacy against *Escherichia coli* at 2.6 V *vs.* RHE.

1 Introduction

Driven by global environmental regulations, interest in carbon-free technologies has continuously intensified, with a particular focus on the sustainable production of hydrogen.[1,2] As a primary feedstock for various chemical syntheses and a high-density energy carrier, hydrogen plays a pivotal role in energy storage systems. Currently, most of the industrial hydrogen is supplied as a by-product from petrochemical processes. However, this route is associated with substantial carbon dioxide emissions. To address this, water electrolysis has emerged as a promising eco-friendly alternative, utilizing renewable electricity to split water.[3,4]

The primary bottleneck in conventional water electrolysis is the sluggish oxygen evolution reaction (OER) at the anode.[5] The OER is hindered by high overpotentials and the indispensable use of expensive noble metal catalysts. Furthermore, the evolved oxygen gas possesses relatively low market value. Consequently, extensive research has shifted toward replacing the OER with value-added oxidation reactions,[6–8] thereby enabling a dual-benefit system that simultaneously generates clean energy at the cathode and performs environmental remediation at the anode. Among these, the electrochemical production of hydrogen peroxide (H_2O_2) is of significant interest. H_2O_2 is a potent oxidant widely utilized in chemical synthesis and wastewater treatment. Notably, H_2O_2 can be efficiently synthesized in $KHCO_3$ electrolytes without complex additives *via* the two-electron water oxidation reaction (2e-WOR).[9] Compared to the four-electron OER, the 2e-WOR is kinetically more favorable due to fewer electron transfer steps, leading to a theoretically lower overpotential.[10,11]

Despite these advantages, the practical application of electro-synthesized H_2O_2 for water treatment faces critical limitations. The inherent oxidation potential of H_2O_2 is relatively modest at 1.76 V *vs.* normal hydrogen electrode (NHE),[12,13] which is often insufficient for the rapid degradation of recalcitrant organic pollutants or the complete inactivation of resilient bacterial strains. As a result, an additional activation step is typically required to generate highly reactive hydroxyl radicals ($^{\cdot}OH$).[14–16] However, conventional heterogeneous Fenton or Fenton-like processes suffer from sluggish interfacial reaction kinetics, which significantly restrict radical generation efficiency.[17] Moreover, performing this activation as a separate, subsequent process often involves complex handling and the inherent challenges of stabilizing and transporting unstable H_2O_2.[18] Conventional strategies to accelerate Fenton-like reactions, such as catalyst structure engineering or thermal activation,[19–21] have shown limited success in fundamentally overcoming these kinetic constraints.

Recently, external-field-assisted catalysis has emerged as a promising approach for regulating reaction pathways. Magnetic field-assisted catalysis, in particular, modulates spin-dependent electron transfer processes by aligning electron spins within magnetic materials, which lowers activation energy barriers and accelerates reaction kinetics.[22–24] Significant efficiency gains could be realized if we introduce this new concept to the electrochemical generation of H_2O_2 with its immediate *in situ* activation, thereby eliminating intermediate handling steps while maximizing reactive radical utilization.

[a]Department of Chemistry, Sungkyunkwan University (SKKU), Suwon, Republic of Korea. E-mail: hyoyoung@skku.edu

[b]Institute for Quantum Biophysics (IQB), Sungkyunkwan University (SKKU), Suwon, Republic of Korea

[c]National Institute of Climate and Environment (NICE), Sungkyunkwan University, Suwon, Republic of Korea

† These authors contributed equally to this work.

In this study, we report, for the first time, an integrated system that couples the two-electron water oxidation reaction (2e-WOR) for H_2O_2 production with a magnetic field-enhanced Fenton-like reaction. By coupling the *in situ* production and simultaneous decomposition of H_2O_2 into $^{\bullet}OH$, we achieve a strong synergistic effect for high-efficiency water disinfection. To realize this, we synthesized a unique heterostructure comprising Fe_3O_4 nanospheres decorated with Mn-doped SnO_2. In this architecture, Mn doping modulates the electronic structure of SnO_2, significantly reducing charge transfer resistance to drive continuous H_2O_2 generation, while the Fe_3O_4 serves as the Fenton-like activation center. Notably, an external magnetic field accelerates radical generation at the catalyst interface. This dual-functional system achieves 99.9% bacterial inactivation, offering a new strategy for integrating spin-dependent catalysis with electrochemical systems for sustainable water treatment.

2 Experimental

2.1. Chemicals and materials

$FeCl_3$ (Sigma-Aldrich), $NaAc\cdot 3H_2O$ (Sigma-Aldrich), PEG 2000 (TCI), ethylene glycol, $SnCl_4\cdot 5H_2O$, $MnCl_2\cdot 4H_2O$, DI water, $KHCO_3$, H_2SO_4, $KMnO_4$, terephthalic acid (TA), *Escherichia coli* (ATCC 25922, Kisan Bio, Korea), Luria Bertani broth (*E. coli*, LB, Kisan Bio, Korea).

2.2. Synthesis of Fe_3O_4

The method was adapted from a previously reported procedure.[25] $FeCl_3$ 14.2 mmol, $NaAc\cdot 3H_2O$ 46 mmol, PEG 2000 were dissolved in ethylene glycol 70 mL, and then the solution was stirred overnight. The mixed solution was transferred into a 100 mL Teflon-lined stainless-steel autoclave. The autoclave was sealed and heated to 200 °C for 6 h and then cooled to room temperature. The obtained powder was washed three times with deionized water (DI water) using a magnet and then dried in a vacuum oven at 60 °C overnight.

2.3. Synthesis of Mn-doped SnO_2@Fe_3O_4

Fe_3O_4 7.24 mmol, $SnCl_4\cdot 5H_2O$ 2.8 mmol, $MnCl_2\cdot 4H_2O$ 0.14 mmol and 2.8 mmol PEG 2000 5 mmol were mixed in 20 mL DI water, and then the solution was stirred for 30 min. NaOH 32 mmol and DI water 15 mL were added to the mixed solution. The mixed solution was transferred into a 100 mL Teflon-lined stainless-steel autoclave. The autoclave was sealed and heated to 180 °C for 10 h and then cooled to room temperature. The obtained powder was washed three times with DI water using a magnet and then dried in a vacuum oven at 60 °C overnight.

2.4. Synthesis of SnO_2@Fe_3O_4

The synthesis was conducted following the same procedure as that of Mn-doped SnO_2@Fe_3O_4, but without the addition of $MnCl_2\cdot 4H_2O$.

2.5. Materials characterization

The crystalline structure of the catalysts was determined by X-ray diffraction (XRD) on a Rigaku SmartLab (Cu-Kα source with λ of 0.15406 nm). The elemental composition of the material was analyzed by using a PerkinElmer Avio 550 Max ICP-OES spectrometer. The morphology of the catalyst was characterized by scanning electron microscope (SEM) JEOL JSM-7100F and transmission electron microscope (TEM) on JEOL JEM-F200 at 200 kV, element composition and distribution by energy dispersive X-ray spectroscopy (EDS) element mappings. X-ray photoelectron spectroscopy (XPS) was performed to characterize the electronic structures of the catalyst on NEXSA G2 with an Al Kα X-ray source (1.4866 keV).

2.6. Electrocatalytic analysis

All the electrochemical data were collected on a Zive SP-1 potentiostat (Wonatech). Catalytic performance was conducted in 2 M $KHCO_3$ with a 3-electrode system. The catalyst ink, 5 mg of the catalyst powder, was dispersed into the solution, including 490 μL of IPA, 490 μL of DI water, and 20 μL of Nafion (5 wt%). The mixed solution was sonicated for 1 h. Then, 50 μL of the catalyst ink was loaded on 0.5 × 0.5 cm^2 carbon paper as the working electrode. The Ag/AgCl as the reference electrode and the Pt mesh as the counter electrode were used. The concentration of produced H_2O_2 was determined *via* potentiometric titration using a potassium permanganate $KMnO_4$ solution. The redox reaction is as follows:

$$2KMnO_4 + 5H_2O_2 + 3H_2SO_4 \rightarrow 2MnSO_4 + 5O_2 + 8H_2O + K_2SO_4$$

In a typical titration, the reaction solution was titrated with 0.02 M $KMnO_4$ in the presence of 1 mL of 3 M H_2SO_4 until the light pink endpoint was reached.[26]

To determine the faradaic efficiency (FE) of hydrogen, we employed the water displacement method.[27] The FE was evaluated at potentials ranging from 2.0 to 3.0 V *vs.* RHE for durations of 5, 10, and 15 min.

$$\text{Faradaic efficiency} = znF/Q$$

where z is the number of electrons transferred, n is the number of moles of the product produced, F is the Faraday constant (96 485 C mol^{-1}), Q is total charge.

To detect $^{\bullet}OH$, radical probe experiments were conducted by adding 12 mM terephthalic acid (TA) to the 2 M $KHCO_3$ electrolyte. The reaction between TA and $^{\bullet}OH$ to form the fluorescent product, 2-hydroxyterephthalic acid (2-HTA), proceeded according to the following equation:

$$C_6H_4(COOH)_2 + {}^{\bullet}OH \rightarrow C_6H_3(OH)(COOH)_2 + {}^{\bullet}H$$

The resulting 2-HTA was analysed by using PL spectroscopy, with its characteristic fluorescence signal being monitored at an emission wavelength of 425 nm.

2.7. Antibacterial experiments

For antibacterial experiments, *E. coli* was incubated in Luria Bertani broth at 37 °C with 200 rpm agitation for 12 h (shaking incubator, LI-BS100, LK LAB KOREA, Korea). Then, the optical density of bacterial suspension was measured at 600 nm (OD_{600}) to determine the number of bacteria using ultra-visible (UV-vis) spectroscopy and diluted to the final concentration of 2×10^6 CFU mL^{-1} with a 2 M $KHCO_3$ in phosphate-buffer saline (PBS, 1×, Sigma Aldrich, USA) solution. The prepared bacterial suspension (20 mL) was added to a cell containing the catalytic electrode (1 mg mL^{-1}). The reaction was conducted at 2.6 V *vs.* reversible hydrogen electrode (RHE) at room temperature. At each time, 100 μL of an aliquot from the reaction suspension was diluted 2 times (10^{-2}) followed by 100 μL aliquot was spread on an LB agar plate. After incubation at 37 °C for 12 h, the colony-forming unit of bacteria was estimated using the standard-counting method.

3 Results and discussion

3.1. Structure characterization

The Fe_3O_4 nanospheres were synthesized *via* a hydrothermal method, followed by a subsequent hydrothermal process to grow either SnO_2 or Mn-doped SnO_2, resulting in SnO_2@Fe_3O_4 (TOFO) and Mn-SnO_2@Fe_3O_4 (MTOFO) heterostructures, respectively. To investigate the crystalline structure of the prepared catalysts, XRD analysis was performed. Fig. 1a shows the XRD patterns of TOFO and MTOFO, which clearly exhibit the characteristic peaks of Fe_3O_4. These peaks remain well-preserved after the incorporation of SnO_2, while the emergence of new diffraction peaks corresponding to SnO_2 confirms the successful formation of the SnO_2@Fe_3O_4 heterostructure. Furthermore, a discernible peak shift in the SnO_2 diffraction lines was observed following Mn-doping, indicating the successful integration of Mn ions into the SnO_2 lattice.[28] To quantitatively verify the successful doping of Mn, ICP-OES analysis was performed, with the results presented in Fig. S1. The detected Mn content of 0.46 wt% provides quantitative support for the structural shifts observed in XRD.

The morphological evolution was further examined through SEM, as shown in Fig. 1b and S2. The pristine Fe_3O_4 displayed a uniform nanospherical morphology, which was maintained even after the secondary growth of the SnO_2 layers. For a more detailed structural analysis, HR-TEM was employed. The low-magnification TEM images corroborated the SEM findings, showing well-defined nanospherical structures.

At higher magnification, Fig. 1c and S3, S4 reveal the lattice fringes and the interfacial relationship within the heterostructure. The measured *d*-spacings of 0.34 and 0.49 nm correspond to the (110) facet of SnO_2 and the (111) facet of Fe_3O_4, respectively.[29,30] These findings further substantiate the successful construction of the heterojunction between the two

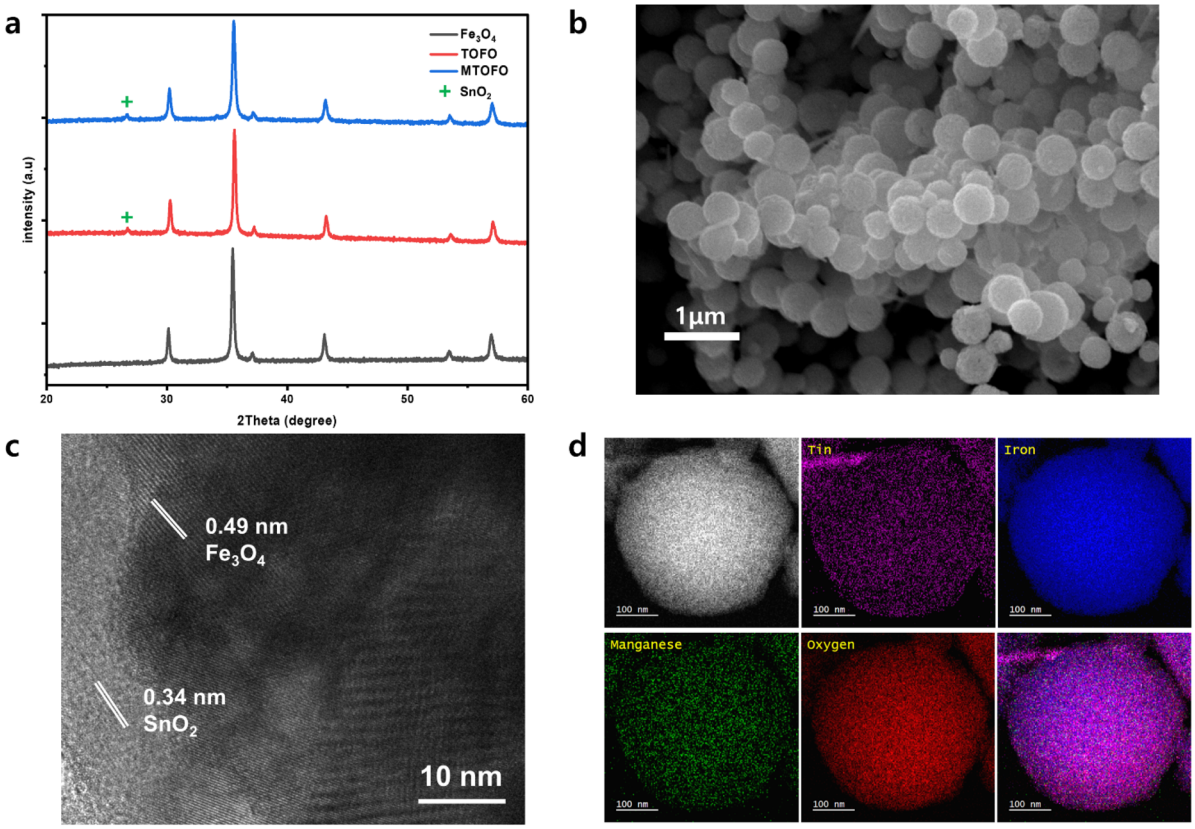

Fig. 1 Characterization of crystal structure and morphology: (a) XRD patterns of Fe_3O_4, TOFO, MTOFO. (b) SEM image of MTOFO. (c) HR-TEM image of MTOFO. (d) HAADF-STEM images of MTOFO and EDS corresponding elemental and mixed mapping.

phases. Finally, Fig. 1d and S5 shows the elemental distribution through scanning transmission electron microscopy (STEM)-EDS mapping. The elemental maps demonstrate that Mn and Sn are uniformly distributed over the surface of the Fe_3O_4, confirming the successful synthesis of the Fe_3O_4 nanospheres decorated with Mn-doped SnO_2.

XPS was conducted to investigate the electronic structures of the synthesized catalysts. As shown in the Sn 3d spectra of Fig. 2a, the binding energies for Sn^{4+} and Sn^{2+} in the Sn $3d_{5/2}$ state of the pristine TOFO were observed at 487.9 and 487.0 eV, respectively.[31,32] Following Mn doping, these peaks shifted to lower binding energies of 487.5 and 486.4 eV. A similar negative shift was observed in the Sn $3d_{3/2}$ spectra, where the Sn^{4+} and Sn^{2+} peaks moved from 496.6 and 495.7 eV to 496.0 and 495.4 eV, respectively. Furthermore, the successful incorporation of Mn was confirmed by the Mn 2p XPS peaks provided in Fig. S6.

Fig. 2b displays the high-resolution Fe 2p XPS spectra. Notably, the Fe^{3+} signal is split into two distinct peaks corresponding to the tetrahedral and octahedral sites, which is a characteristic feature of Fe_3O_4. For the pristine TOFO, the Fe $2p_{3/2}$ peaks assigned to Fe^{2+}, octahedral Fe^{3+} (Fe_{oct}^{3+}), and tetrahedral Fe^{3+} (Fe_{tetra}^{3+}) were located at 710.0, 711.4, and 712.6 eV, respectively.[33] In the MTOFO catalyst, these peaks shifted to 710.0, 711.2, and 712.4 eV. This shift to lower binding energies is attributed to electron transfer from the Mn-doped SnO_2, driven by its relatively lower oxidation state. Correspondingly, in the Fe $2p_{1/2}$ spectra, the peaks for Fe^{2+}, Fe_{oct}^{3+}, and Fe_{tetra}^{3+} shifted from 723.0, 724.2, and 725.7 eV to 723.3, 724.4, and 725.3 eV. Finally, the O 1s XPS spectra revealed an increase in the proportion of the surface hydroxyl (–OH) peak in Fig. S7.

3.2. Electrocatalytic performance

The electrochemical evaluations were conducted using a three-electrode system to investigate the influence of an external magnetic field on catalytic performance in Fig. S8. As shown in Fig. 3a, linear sweep voltammetry (LSV) revealed that all catalysts exhibited similar onset potentials at 1.7 V *vs.* RHE. Notably, the MTOFO catalyst under a magnetic field achieved the highest current density. Analysis of the Tafel slopes in Fig. 3b showed that peaks were distributed at similar positions regardless of the magnetic environment. Interestingly, Mn-doping led to a reduction in the Tafel slope at consistent potentials, suggesting that while the magnetic field influences the reaction at the onset, the Mn-dopants fundamentally enhance the intrinsic catalytic reactivity.

Electrochemical impedance spectroscopy (EIS) further confirmed this enhancement, where Fig. 3c demonstrates that Mn-doping reduced the charge transfer resistance (R_{ct}) from 4 ohm for TOFO to 3 ohm for MTOFO. The electrochemically active surface area (ECSA) measurements, as shown in Fig. 3d and S9, yielded double-layer capacitance values of 68 mF cm^{-2} for TOFO and 52 mF cm^{-2} for MTOFO.

Subsequently, H_2O_2 production rates were evaluated as a function of applied potential. Fig. 3e presents that at an applied potential of 2.6 V *vs.* RHE, MTOFO reached a maximum H_2O_2 production rate of 60.2 μmol min^{-1}. Intriguingly, the H_2O_2 yield for MTOFO decreased under specific magnetic conditions, which prompted further investigation into radical generation. It was confirmed that the catalyst exhibits significantly higher efficiency compared to previously reported 2e-WOR catalysts, as summarized in Table S1.

In addition, the faradaic efficiency (FE) of MTOFO was measured within the potential range of 2.0–3.0 V *vs.* RHE to quantify the hydrogen production. A high FE of over 90% was consistently observed across all measured potentials in Fig. S10 and S11. Finally, long-term stability tests at 2.6 V confirmed that the catalyst maintained robust performance for over 15 h in 2 M $KHCO_3$ in Fig. 3f. Finally, long-term stability tests at 2.6 V confirmed that the catalyst maintained robust performance for over 15 h in 2 M $KHCO_3$ in Fig. 3f. Furthermore, to evaluate operational stability under practical conditions, the durability was tested at 2.6 V *vs.* RHE in tap water, both with and without the addition of 2 M $KHCO_3$. The catalyst exhibited sustained stability for over 15 h and 35 h, respectively, as shown in Fig. S12.

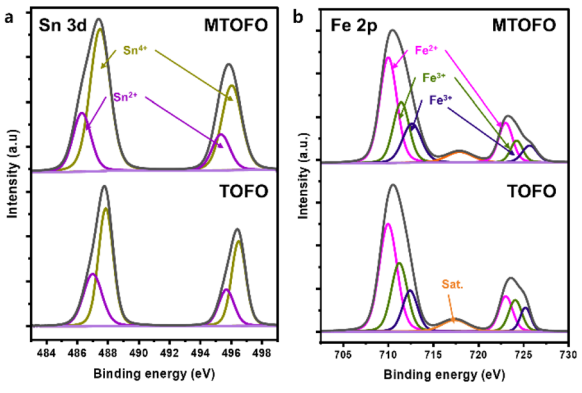

Fig. 2 Characterization of electronic structure: (a) XPS analysis of TOFO, MTOFO electrocatalysts in terms of Sn 3d. (b) Fe 2p.

3.3. Electrochemical radical probe and bacterial disinfection

To elucidate the observed decrease in H_2O_2 production under magnetic fields, we hypothesized that H_2O_2 was being consumed to generate $^{\bullet}OH$. A radical probe experiment was performed using 12 mM TA in a $KHCO_3$ electrolyte at 2.6 V *vs.* RHE.[34,35] During the initial 30 min, the photoluminescence (PL) peaks at 425 nm saturated at a consistent level regardless of the magnetic field in Fig. 4a. However, after 1 h, only the catalyst that reacted under the magnetic field showed a significant increase in PL intensity. The magnetic field facilitates a Fenton-like reaction and the production of $^{\bullet}OH$ for 2-HTA formation, a kinetic acceleration which is primarily attributed to the synergistic effect of spin-state regulation and structural modulation of radical intermediates. Theoretically, radicals are generated as pairs in either singlet (S) or triplet (T) configurations.[36] In the absence of a magnetic field, singlet radical pairs (*e.g.*, $^1[HO^{\bullet}\uparrow\cdots\downarrow{}^{\bullet}OH]$) tend to rapidly recombine into H_2O_2 due to the Pauli exclusion principle, thereby limiting the steady-

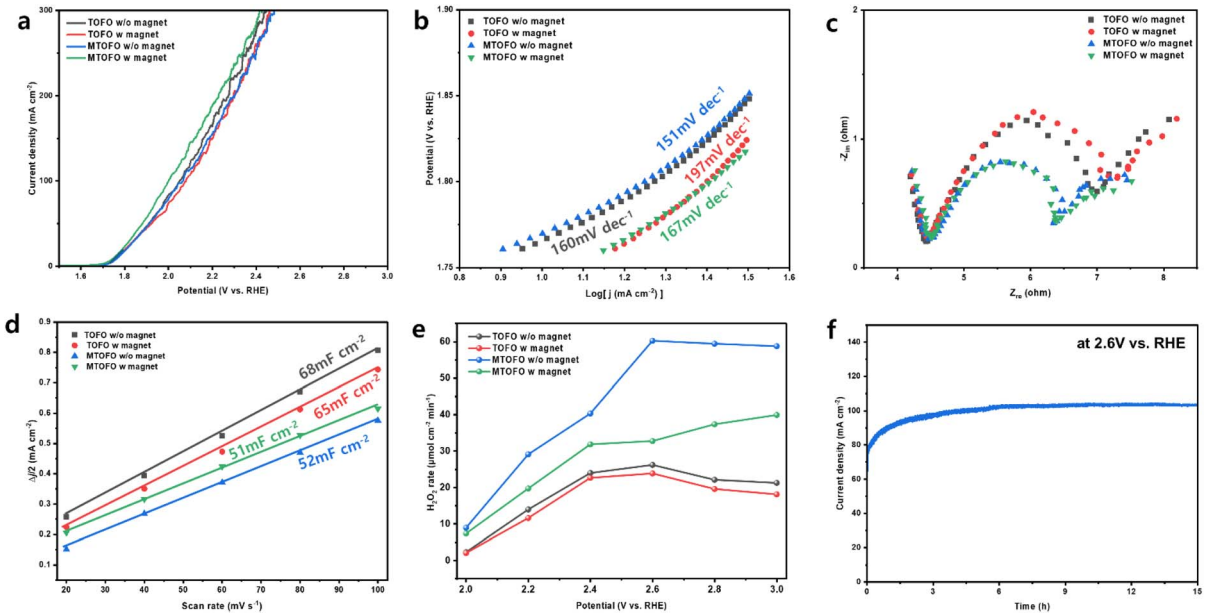

Fig. 3 Electrocatalytic performance (a) polarization curves of the TOFO and MTOFO with(out) magnet. (b) Tafel plot and (c) Nyquist plot at 1.8 V *vs.* RHE in 2 M $KHCO_3$. (d) ECSA of each catalyst and with(out) magnet. (e) H_2O_2 yields at various applied potentials. (f) Stability of MTOFO at 2.6 V *vs.* RHE.

state concentration of active species.[37] The application of an external magnetic field induces Zeeman energy splitting of the triplet sublevels, which effectively promotes S → T intersystem crossing while suppressing the T → S evolution.[38,39] Given that the recombination of triplet radical pairs is spin-forbidden, these species exhibit a significantly higher dissociation probability, allowing a greater population of free radicals to escape and participate in the Fenton-like reaction, which effectively lowers the apparent activation energy. Furthermore, literature suggests that the external field acts as an equivalent force that

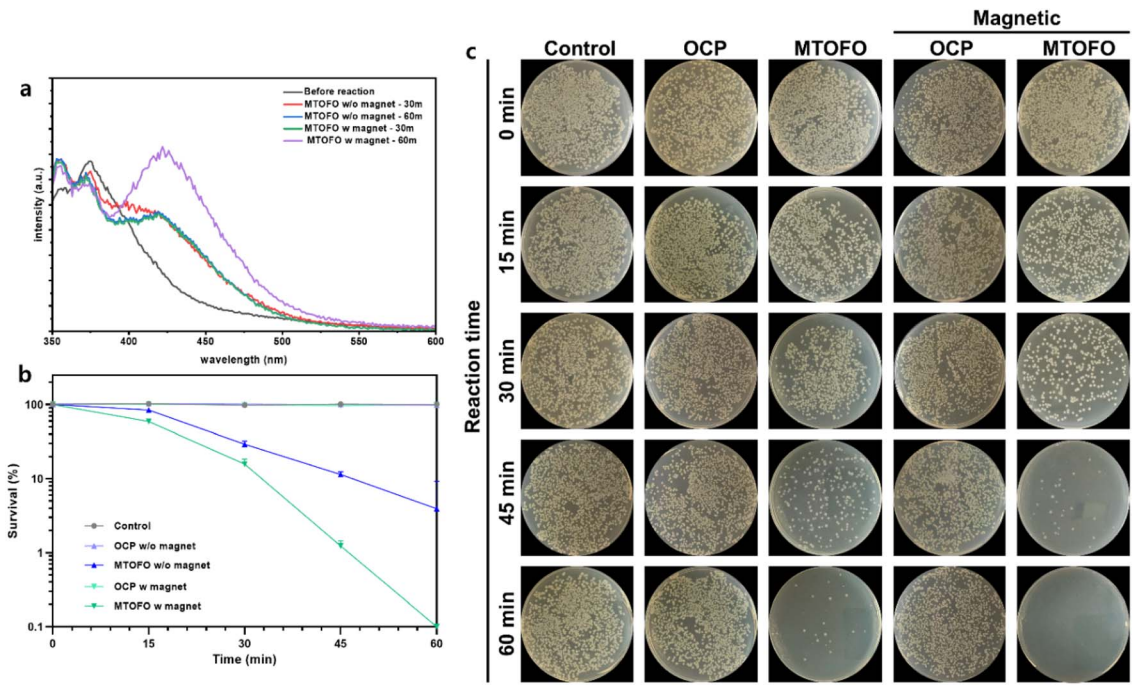

Fig. 4 Radical probe and antibacterial test (a) PL spectra of TA probe test for 30 m and 60 m. (b) Time-dependent log-reduction of bacteria in 2 M $KHCO_3$ for MTOFO with (out) magnet ($n = 3$ independent experiments per bacterial concentration). (c) Bacterial colonies images during antibacterial experiments using 2 M $KHCO_3$.

lengthens O–O and O–H bonds in H_2O_2, further reducing the energy barrier for bond scission and facilitating the observed kinetic promotion and efficient H_2O_2 utilization.[40]

This radical generation mechanism was further applied to water disinfection. Before the antibacterial experiments, the electrolyte concentrations were optimized to exclude antibacterial effects originating from the electrolyte in Fig. S13. Antibacterial experiments were conducted against *E. coli*, a representative Gram-negative bacterium. While control experiments at open circuit potential (OCP) showed no significant impact on bacterial survival, MTOFO achieved a 96.1% antibacterial rate at 2.6 V *vs.* RHE. Remarkably, the synergistic combination of an applied potential of 2.6 V and a magnetic field enhanced the antibacterial activity of MTOFO to 99.9% in Fig. 4b and c. These values represent significantly higher efficiency compared to previously reported catalysts for bacterial disinfection, as summarized in Table S2. These results demonstrate that the synergy between electric current and magnetic fields enables MTOFO to efficiently generate H_2O_2 and subsequently convert it into highly reactive $^{\bullet}OH$, achieving superior disinfection of high-concentration bacteria.

4 Conclusions

In summary, we successfully achieved simultaneous hydrogen and hydrogen peroxide production *via* a 2e-WOR using a Mn-doped SnO_2@Fe_3O_4 electrocatalyst with magnet. Going beyond conventional 2e-WOR, the incorporation of Fe_3O_4 enabled the generation of highly reactive $^{\bullet}OH$ through an electro-Fenton-like process. Furthermore, TA probe assays confirmed that the application of an external magnetic field significantly enhanced this Fenton-like reactivity. The generated $^{\bullet}OH$ were effectively utilized for bacterial disinfection, demonstrating meaningful results for water purification. We believe that this dual-functional system, concurrently producing clean H_2 and potent $^{\bullet}OH$, presents a promising new strategy for advanced wastewater treatment. Future studies will focus on implementing this system in more complex, real-world environmental matrices.

Author contributions

Y. H. and J. C. conceived and designed the studies and wrote the paper. Y. H. and S. O. synthesized the materials, performed electrochemical experiments, and PL. H. K. supported the characterization and SEM analysis. H. L. provided direction, supervision, and editing of this paper.

Conflicts of interest

There are no conflicts to declare.

Data availability

The data that support the findings of this study are available in the supplementary information (SI) of this manuscript. Supplementary information: additional ICP-OES data, SEM, TEM, and STEM-EDS images, and XPS Mn 2p and O 1s spectra; stability tests conducted with tap water, the cell setup image, faradaic efficiency of hydrogen, and the viability of *E. coli* depending on $KHCO_3$ concentration. Additionally, summary tables comparing this work with previously published literature are provided. See DOI: https://doi.org/10.1039/d6ta02632j.

Acknowledgements

This work was supported by the National Research Foundation of Korea (NRF) grant funded by the Korean Government (MSIT) (NRF-2022R1A2C2093415) and partially supported by the Korea Basic Science Institute (National Research Facilities and Equipment Center) grant funded by the Ministry of Education (RS-2022-NF000854).

References

1 S. Chu, Y. Cui and N. Liu, *Nat. Mater.*, 2017, **16**, 16–22.
2 J. G. Segovia-Hernández, S. Hernández, E. Cossío-Vargas, M. Juarez-García and E. Sánchez-Ramírez, *RSC Sustain.*, 2025, **3**, 134–157.
3 S. A. Ansari, *Fuel*, 2026, **404**, 136252.
4 M. Rezaei, A. Nezamzadeh-Ejhieh and A. R. Massah, *Mater. Today Energy*, 2025, **48**, 101754.
5 J. Choi, S. Seo, M. Kim, Y. Han, X. Shao and H. Lee, *Small*, 2024, **20**, 2304560.
6 Y. Yang, J. Liu, M. Ahmad, X.-Q. Sun, C. Liu, S. Chen, J. Zhang, J.-L. Luo and X.-Z. Fu, *Chem. Eng. J.*, 2025, **505**, 159653.
7 H. Sun, X. Xu, L. Fei, W. Zhou and Z. Shao, *Adv. Energy Mater.*, 2024, **14**, 2401242.
8 Y. Song, J. Qian, S. Li, Z. Zhao, H. Chen, K. Zou, Z. Han, Z. Li, H. Li and H. Zhou, *Angew. Chem.*, 2025, **137**, e202502847.
9 S. Y. Park, H. Abroshan, X. Shi, H. S. Jung, S. Siahrostami and X. Zheng, *ACS Energy Lett.*, 2018, **4**, 352–357.
10 C. B. Guta, H. G. Edao, W. B. Dilebo, C.-Y. Chang, F. T. Angerasa, E. A. Moges, Y. Nikodimos, K. Lakshmanan, M.-C. Tsai and W.-N. Su, *Chem. Eng. J.*, 2024, **500**, 156418.
11 A. Izgorodin, E. Izgorodina and D. R. MacFarlane, *Energy Environ. Sci.*, 2012, **5**, 9496–9501.
12 J. Choi, S. Lee, H. Ko, J. Kim, S. Seo, S. Noh, T. Kim, S. Perumal, Y. Han and S. Joung, *Nano Lett.*, 2025, **25**, 17211–17219.
13 F. Vatansever, W. C. de Melo, P. Avci, D. Vecchio, M. Sadasivam, A. Gupta, R. Chandran, M. Karimi, N. A. Parizotto and R. Yin, *FEMS Microbiol. Rev.*, 2013, **37**, 955–989.
14 S. Gao, G. He, B. Wang, Q. Li, X. Chen, D. Mei and J. Yu, *J. Am. Chem. Soc.*, 2025, **147**, 35975–35984.
15 H. Li, X. Zheng, J. Li, T. Liu, M. Liu, J. Wu, W. Liu and P. Wang, *J. Am. Chem. Soc.*, 2026, **148**(4), 4110–4125.
16 Y.-Y. Zhang, M.-J. Hou, W.-C. Chen, G.-G. Shan, K.-Z. Shao, C.-Y. Sun, C. Qin, X.-L. Wang and Z.-M. Su, *J. Am. Chem. Soc.*, 2026, **148**, 8535–8545.

17 E. Brillas, I. Sirés and M. A. Oturan, *Chem. Rev.*, 2009, **109**, 6570–6631.
18 I. Sirés, E. Brillas, M. A. Oturan, M. A. Rodrigo and M. Panizza, *Environ. Sci. Pollut. Res.*, 2014, **21**, 8336–8367.
19 C. Cheng, W. Ren, F. Miao, X. Chen, X. Chen and H. Zhang, *Angew. Chem., Int. Ed.*, 2023, **62**, e202218510.
20 F. Zhang, X. Li, D. Wang, X. Wu, L. Niu, Y. Li, P. Zhang, H. Zhu, J. Xin and X. Li, *Appl. Catal. B Environ. Energy*, 2025, **365**, 124923.
21 C. Jia, Y. Guo and F. G. Wu, *Small*, 2022, **18**, 2103868.
22 X. Jiang, Y. Chen, X. Zhang, F. You, J. Yao, H. Yang and B. Y. Xia, *ChemSusChem*, 2022, **15**, e202201551.
23 J. B. Chen, J. Ying, Y. Tian, Y. X. Xiao and X. Y. Yang, *Adv. Funct. Mater.*, 2025, **35**, 2415660.
24 Y. Zhang, C. Liang, J. Wu, H. Liu, B. Zhang, Z. Jiang, S. Li and P. Xu, *ACS Appl. Energy Mater.*, 2020, **3**, 10303–10316.
25 Z. Deng, S. He, W. Wang, M. Xu, H. Zheng, J. Yan, W. Zhang, J. Yun, W. Zhao and P. Gan, *J. Magn. Magn. Mater.*, 2020, **498**, 166224.
26 C. B. Guta, C.-Y. Chang, F. T. Angerasa, B. D. Bejena, H. G. Edao, W. B. Dilebo, E. A. Moges, M.-C. Tsai, W.-N. Su and B. J. Hwang, *Chem. Eng. J.*, 2025, 169336.
27 X. Fu, D. Cheng, A. Zhang, J. Zhou, S. Wang, C. Wan, X. Zhao, J. Chen, P. Sautet and Y. Huang, *Angew. Chem., Int. Ed.*, 2025, **64**, e202503828.
28 U. Choudhari and S. Jagtap, *AIP Adv.*, 2021, **11**, 125327.
29 S. P. Kim, M. Y. Choi and H. C. Choi, *Mater. Res. Bull.*, 2016, **74**, 85–89.
30 B. S. Yadav, R. Singh, A. K. Vishwakarma and N. Kumar, *J. Supercond. Novel Magn.*, 2020, **33**, 2199–2208.
31 M. Kumar, V. Bhatt, A. Abhyankar, J. Kim, A. Kumar, S. H. Patil and J.-H. Yun, *Sci. Rep.*, 2018, **8**, 8079.
32 J. W. Song, Y. S. Shin, M. Kim, J. Lee, D. Lee, J. Seo, Y. Lee, W. Lee, H. B. Kim and S. I. Mo, *Adv. Energy Mater.*, 2024, **14**, 2401753.
33 J. M. Cho, M. H. Jeong and J. W. Bae, *Res. Chem. Intermed.*, 2016, **42**, 335–350.
34 N. T. Hoang and F. M. Mwazighe, *Mosc. Univ. Chem. Bull.*, 2022, **77**, 286–299.
35 Y. Jing and B. P. Chaplin, *Environ. Sci. Technol.*, 2017, **51**, 2355–2365.
36 C. T. Rodgers and P. J. Hore, *Proc. Natl. Acad. Sci. U. S. A.*, 2009, **106**, 353–360.
37 H. Pan, X. Jiang, X. Wang, Q. Wang, M. Wang and Y. Shen, *J. Phys. Chem. Lett.*, 2019, **11**, 48–53.
38 B. Brocklehurst, *Chem. Soc. Rev.*, 2002, **31**, 301–311.
39 H. Pan, M. Wang, Y. Shen and B. Hu, *J. Phys. Chem. C*, 2018, **122**, 19880–19885.
40 H. Dan, Y. Kong, Q. Yue, J. Liu, X. Xu, W. Kong, Y. Gao and B. Gao, *Chem. Eng. J.*, 2021, **420**, 127634.

